

2 EXPERIMENTAL DETAILS

2.1 THREE-WAVE MIXING AS AN INFRARED SOURCE

Three-wave mixing is a versatile method for generating short and tuneable pulses at wavelengths ranging from ultraviolet (~ 250 nm) to mid-infrared (up to ~ 10 μm). Examples of three-wave mixing are sum-frequency generation (SFG), second-harmonic generation (SHG), difference-frequency generation (DFG), and optical parametric generation and amplification (OPG and OPA). These techniques^{23,24,27,34,48,56,69,97} are now standard practice in time-resolved spectroscopy. In these processes, oscillating electrical fields at two or three different frequencies are coupled to each other.

In general, the dielectric polarization $P(t)$ at time t in a medium can be written as a power series in the electrical field:

$$P(t) \propto \chi^{(1)}E(t) + \chi^{(2)}E^2(t) + \chi^{(3)}E^3(t) + \dots \quad (2.1)$$

Here, the coefficients $\chi^{(n)}$ are the n -th order susceptibilities of the medium. For any three-wave mixing process, the second-order term is crucial; it is only nonzero in media that have a broken inversion symmetry. If we write

$$E(t) = E_1e^{i\omega_1t} + E_2e^{i\omega_2t} + \text{c.c.}, \quad (2.2)$$

where c.c. denotes the complex conjugate, the second-order term in Eq. (2.1) will read^d

$$P^{(2)}(t) \propto \sum \chi^{(2)} n_o E_1^{n_1} E_2^{n_2} e^{i(m_1\omega_1 + m_2\omega_2)t} + \text{c.c.}, \quad (2.3)$$

where the summation is over

$$(n_o, n_1, n_2, m_1, m_2) = (1, 2, 0, 2, 0), (1, 0, 2, 0, 2), (2, 2, 0, 0, 0), \\ (2, 0, 2, 0, 0), (2, 1, 1, 1, -1), (2, 1, 1, 1, 1). \quad (2.4)$$

The six combinations (n_x, m_x) correspond, respectively, to the second harmonic of E_1 , the second harmonic of E_2 , the optically rectified signals of E_1 and E_2 , the difference frequency, and the sum frequency. A medium that is thus pumped by the fields E_1 and E_2 will radiate a field E_3 with an angular frequency $\omega_3 = m_1\omega_1 + m_2\omega_2$.

Up to now, we ignored the position dependence of the electrical fields. In a typical situation, the electrical fields are traveling waves with an electric field

$$E_j(\mathbf{x}, t) = e^{i(\omega_j t - \mathbf{k}_j \cdot \mathbf{x})}, \quad (2.5)$$

^dWe assume here that $\chi^{(2)}$ is a scalar. In reality, $\chi^{(2)}$ is a tensor whose components depend on the combination of frequencies.¹⁰⁹

at position \mathbf{x} , with the wave vector $\mathbf{k}_j = n(\omega_j)\omega_j/c$, where c is the velocity of light and $n(\omega_j)$ the index of refraction of the medium at angular frequency ω_j . Thus, the second-order polarization angular frequency ω_3 is

$$P^{(2)}(\mathbf{x}, t) \propto E_1^{n_1} E_2^{n_2} e^{i(\omega_3 t - (m_1 \mathbf{k}_1 + m_2 \mathbf{k}_2) \cdot \mathbf{x})}. \quad (2.6)$$

At each position \mathbf{x} , the oscillating second-order polarization radiates at angular frequency ω_3 and a corresponding wave vector $\mathbf{k}_3 = n(\omega_3)\omega_3/c$. Constructive interference, and therefore a high intensity ω_3 field, will occur only if

$$\mathbf{k}_3 = m_1 \mathbf{k}_1 + m_2 \mathbf{k}_2. \quad (2.7)$$

Equation (2.7) is known as the phase *phase matching condition*. Typically, three-wave mixing is done in a birefringent crystalline material (i.e. the index of refraction depends on the polarization and direction of the light that passes through), where the polarizations of the fields and the orientation of the crystal are chosen such that the phase-matching condition is fulfilled. For more details, see for example Refs. 6, 23, 109, 136.

2.1.1 PARAMETRIC GENERATION AND AMPLIFICATION

Optical parametric amplification (OPA) is a special case of difference frequency generation ($\omega_3 = \omega_1 - \omega_2$), where the pump field amplitude E_1 is much larger than E_2 . The field E_3 that is generated causes, in turn, E_2 to increase by the simultaneous DFG process $\omega_2 = \omega_1 - \omega_3$. Because phase matching for the generation of ω_3 implies phase matching for the generation of ω_2 , light at frequencies ω_2 and ω_3 is generated simultaneously. The latter means that in OPA, a photon at frequency ω_1 is ‘split’ into two photons at frequencies ω_2 and ω_3 . The two fields at frequencies ω_2 and ω_3 are usually referred to as signal (the one with the higher frequency) and idler (the lower frequency), and the field at ω_1 is called the pump (not to be confused with the term ‘pump’ in a pump–probe experiment). Parametric generation (OPG) is the limiting case where, initially, $E_2 = E_3 = 0$. Though Eq. (2.3) suggests that second-order polarizations at neither ω_2 nor ω_3 would be generated, the latter does happen in reality, because of quantum-mechanical properties of the electric field. This is, however, beyond the scope of this short summary of three-wave mixing processes. See for example Refs. 6, 109. For all OPG/OPA wavelength conversions that I describe in this thesis, we used specially designed crystals such as β -barium borate (BBO), potassium titanyl phosphate (KTP), lithium niobate (LiNbO₃), and potassium niobate (KNbO₃). These crystals have, due to their crystal symmetry (or the absence thereof), both a nonzero $\chi^{(2)}$ and a strong birefringence, which we employ for phase-matching. In general, the phase-matching can be of ‘type 1’ (pump polarization is perpendicular to both signal and idler), ‘type 2’ (pump and idler polarizations are perpendicular to the signal), or ‘type 3’ (pump and signal polarizations are perpendicular to idler).

The infrared pulses for the time-resolved experiments presented in this thesis were all generated by OPG/OPA processes. However, in Chapter 3, I will discuss a scheme for the generation of infrared pulses by use of a four-wave mixing process, that employs the third-order term in Eq. (2.1).

2.2 PULSE GENERATION FOR PUMP–PROBE EXPERIMENTS

This section treats the methods of infrared-pulse generation that have been used for the experiments in this thesis. In order to study processes that take place on a timescale on the order of one picosecond or less, we need pulses that are (preferably much) shorter than one picosecond. Moreover, in a pump–probe experiment, the pump pulses should be of an intensity that is sufficiently high to induce measurable changes in the absorbance of the sample under study (see §1.2). We have used several different methods of pulse generation, depending on the required wavelengths, on whether or not two simultaneous independently tuneable pulses were needed, and on the available equipment.

2.2.1 TITANIUM-SAPPHIRE AMPLIFIER

The basis of the pulse generation is a commercial titanium–sapphire amplifier, i.e. a laser that delivers pulses at a repetition rate of 1 kHz, a wavelength of ~ 800 nm, and a pulse duration of ~ 100 fs. Two different amplifiers have been used. For the experiments in Chapters 4 and 7, we used a Quantronix 4800 regenerative amplifier with a pulse energy of 1 mJ, a pulse duration of 150 fs full width at half maximum (FWHM), and a wavelength centered at 800 nm. For the experiments in the remaining chapters, we used a Quantronix Titan regenerative/multipass amplifier with a pulse energy of 3 mJ, a pulse duration of 100 fs (FWHM), and a wavelength centered at 805 nm.

2.2.2 TOPAS: A BBO-BASED OPG/OPA DEVICE

A common element for our pulse generation is the TOPAS. This is a commercial device (manufacturer: Light Conversion, Ltd.) that converts the 800 nm pulses from the Ti:sapphire amplifier to longer wavelengths through a type-2 OPG/OPA (§2.1.1) process. It uses a β -barium borate (BBO) crystal as the nonlinear medium. The output pulses are tunable in the range 1140–1600 nm (signal) and 1600–2650 nm (idler). The wavelength tuning range for both signal and idler is limited by absorption in the BBO crystal of (idler) wavelengths beyond 2500 nm. Since spectroscopic experiments on the OH stretch vibration require wavelengths in the range 2850–3600 nm, additional conversion steps are necessary. A direct conversion by use of a crystal such as KTP (see following sections) instead of BBO is not possible, because it would not survive the high pump intensity required by the first (OPG) step in the conversion.

2.2.3 PULSE GENERATION ($\sim 3 \mu\text{M}$) FOR ONE-COLOR EXPERIMENTS

This section describes the pulse generation for the experiments in Chapters 4 and 7. In these experiments, pump and probe pulses had equal frequencies, hence the name ‘one-color’.

The method of pulse generation is depicted schematically in Fig. 2.1. A Ti:sapphire amplifier (§2.2.1) pumps a Topas OPG/OPA device (§2.2.2). We tuned the Topas to generate a signal wavelength of 1140 nm, with an FWHM bandwidth of 80 nm. The spectrum of this signal contains sufficient intensity at a wavelength of 1090 nm in order to act as a seed for a second OPA process in a potassium titanyl phosphate (KTP) crystal, that is pumped by the remaining 800 nm light. This second OPA process generates a signal at approximately

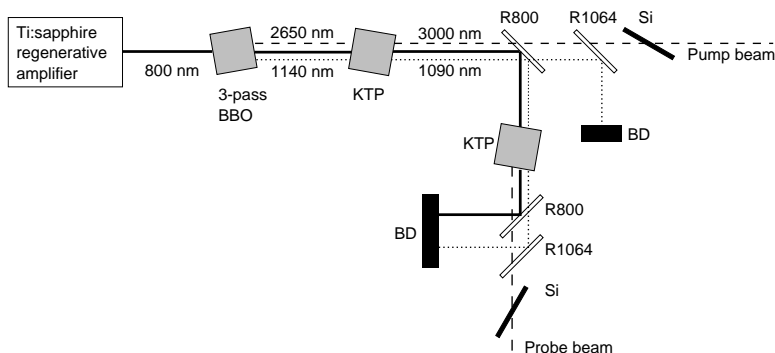


FIGURE 2.1. Generation of mid-infrared pulses for one-color experiments and some of the two-color experiments. Abbreviations: BBO: BBO crystal; KTP: KTP crystal; R800: dielectric 800 nm mirror; R1064: dielectric 1064 nm mirror; Si: silicon Brewster window; BD: beam dump. The probe branch was only used for the experiments in Chapter 4.

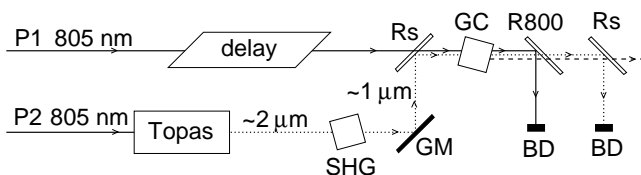


FIGURE 2.2. Pulse generation for §2.2.4 and §2.2.5. Abbreviations: Topas, commercial OPG/OPA device; SHG, second harmonic generation crystal (BBO); GM, gold mirror; Rs, dichroic signal-reflecting mirror; GC, IR-generating crystal (KTP, LiNbO₃, or KNbO₃); R800, dielectric 800-nm mirror. Pump pulse energy at P1, P2 varies; see §2.2.4 and §2.2.5.

1090 nm and an idler at approximately 3000 nm. By changing the phase-match angle of the KTP crystal, the idler wavelength can be continuously tuned up to 3300 nm with an energy of typically 20 μJ , a bandwidth of 80 nm and an FWHM duration of 250 fs. This wavelength range corresponds to frequencies larger than 3000 cm^{-1} , which is suitable for exciting and probing the O–H stretch vibration in water. The remaining 800-nm pump and signal wavelength components are removed by means of dielectric 800 and 1064 nm mirrors. Any remaining short wavelength components are filtered out by a silicon plate positioned at the Brewster angle. This method of infrared pulse generation is described in more detail in Ref. 27. To obtain a probe pulse, we used a reflection from a wedged calcium fluoride window.

2.2.4 PULSE GENERATION ($\sim 3 \mu\text{M}$) FOR TWO-COLOR EXPERIMENTS

In the two-color experiments described in Chapter 4, the pump pulses were generated as described in §2.2.3. Part of the seed and the remaining energy of the 800 nm pulses were combined in a second KTP crystal for an independently frequency-tunable probe pulse with an energy of $< 1 \mu\text{J}$.

In the two-color experiments described in Chapters 6 and 8, the pump and probe

pulses were generated in two completely independent branches. Each branch was set up as in Fig. 2.2. A Topas device (§2.2.2), pumped at 805 nm, delivered idler pulses around $2.2 \mu\text{m}$, which were frequency-doubled in a BBO crystal. The resulting $1.1\text{-}\mu\text{m}$ pulses served as a seed in a type-2 OPA process (§2.1.1) in a 5-mm KTP crystal that was pumped by an independent 805 nm pulse. After the KTP crystal, dielectric mirrors and a long wave pass filter filtered out the remaining 805 nm and signal light. In the pump-pulse branch, the energies of the 805-nm pulses were 0.8 mJ (P1) and 1.3 mJ (P2), which resulted in typical energies of the generated pulses near $3 \mu\text{m}$ of $10\text{--}20 \mu\text{J}$. In the probe-pulse branch, they were 0.45 mJ (P1) and 0.11 mJ (P2), yielding $\sim 1 \mu\text{J}$ of pulse energy. Compared to the method described in §2.2.3, this method offers a much better pulse stability. Typically, the $3 \mu\text{m}$ pulses had a bandwidth of $80\text{--}120 \text{ nm}$ ($80\text{--}100 \text{ cm}^{-1}$) FWHM and a duration of $200\text{--}250 \text{ fs}$ (§2.5).

2.2.5 PULSE GENERATION AT $\sim 4 \mu\text{M}$

This section describes the pulse generation for the experiments in on the OD stretch vibration Chapter 5. The OD stretch vibration has typically a frequency of 2500 cm^{-1} , which corresponds to wavelengths around $4 \mu\text{m}$. The pump and probe pulses were generated independently from each other.

PUMP PULSES Figure 2.2 shows the pump-pulse generation setup, which is very similar to that described in §2.2.4. Here, the Topas device (§2.2.2) was pumped with 0.9 mJ pulses and generated idler pulses at a slightly shorter wavelength, around $2.0 \mu\text{m}$. For the parametric amplification, we used a 5-mm KNbO₃ crystal, which is more suitable than KTP for the wavelength range $3.7\text{--}4.25 \mu\text{m}$. The pulses typically had energies of $18 \mu\text{J}$ and bandwidths of 70 nm (44 cm^{-1}) FWHM.

PROBE PULSES We employed two different techniques for probe pulses at wavelengths below and above $4.25 \mu\text{m}$. Below $4.25 \mu\text{m}$, the technique is similar to that for generating the pump pulses, as described in the previous section, but with smaller pulse energies and a LiNbO₃ crystal instead of a KNbO₃ crystal. With LiNbO₃, the spectral shape and pulse energies of the generated light were more stable than with KNbO₃. It was pumped with 0.1 mJ 805 nm light. Cross-correlation traces of these pulses with the pump pulses (delay-dependence of sum-frequency generation in a LiIO₃ crystal), had FWHMs of 350 fs and bandwidths of $50\text{--}110 \text{ nm}$ ($30\text{--}70 \text{ cm}^{-1}$).

Wavelengths longer than 4250 nm are absorbed by LiNbO₃, which imposed the need of an alternative pulse generation technique. For these longer wavelengths, we tuned the Topas to generated pulses at $1.36 \mu\text{m}$ (signal) and $1.97 \mu\text{m}$ (idler). The signal and idler pumped a DFG (§2.1) process in a 3-mm AgGaS₂ crystal, which generated pulses with a wavelength of $4.40 \mu\text{m}$. In this case, cross-correlation traces of these pulses with the pump pulses had an FWHM of 600 fs and a bandwidth of 166 nm (85 cm^{-1}).

2.3 SAMPLE

We conducted most pump-probe experiments described in this thesis on samples that consist of a thin ($200\text{--}500 \mu\text{m}$) layer of liquid sandwiched between two 4-mm-thick CaF₂

windows. Calcium fluoride combines a number of properties that make it very suitable for this purpose: it is transparent up to a wavelength of $\sim 8 \mu\text{m}$ (1250 cm^{-1}), practically insoluble, reasonably easy to handle, and not birefringent (which is relevant since the relative polarizations of pump and probe pulses affect the outcome of the experiment). Only for the experiments at low temperatures, described in Chapter 4, we used sapphire windows. Because sapphire is birefringent, we used windows with the optical axis perpendicular to the surface. If the laser pulses do not have a normal angle of incidence, the birefringence still affects the polarization of the pulses. For a small external angle of incidence $\theta = 0.075 \text{ rad}$, a window thickness $L = 3 \text{ mm}$, an ordinary refractive index $n_o = 1.7$,^{58,79} an extraordinary refractive index $(1 + \epsilon)n_o$ with $\epsilon = 0.0011$,[†] and a wavelength (*in vacuo*) $\lambda = 3 \mu\text{m}$, the introduced phase difference between horizontal (p) and vertical (s) polarizations is

$$\Delta\phi \equiv \phi_p - \phi_s \approx \frac{2\pi L \theta^2 \epsilon}{n_o \lambda} = 0.022. \quad (2.8)$$

See for example Refs. 6, 136 for an explanation on calculating effective indices of refraction in birefringent media. For linearly polarized light at an angle of 45 deg (equal p and s components), this phase difference will introduce a polarization component perpendicular to the original polarization with an intensity $\sin^2(\Delta\phi/2) \approx 10^{-4}$ relative to the original intensity, which can safely be neglected. Moreover, in a typical experimental geometry, only the ratio of the intensities of the p and s components is relevant, which is not affected by a phase retardance. (Similarly, any p–s phase differences caused by mirrors can be ignored.)

In the measurements as a function of temperature, described in Chapter 4 and 7, it was important to have a well-defined temperature in the sample. For that reason, we used a construction that rotates the sample in a plane parallel to the sample windows, such that a fresh part of the sample was probed for each laser shot. This limited the temperature error to the effect of one pump pulse, which we can estimate to be less than 0.2 K, assuming that $20 \mu\text{J}$ of energy are homogeneously dissipated in the $200^2 \times 500 \mu\text{m}^3$ focus. We used the rotating sample cell for the experiments in Chapter 5 as well, because the thinner, i.e. $50 \mu\text{m}$, sample would suffer from a larger temperature increase for the same amount of dissipated pump pulse energy. In §2.8, I will discuss the effect the pump pulses heating the sample for a nonmoving sample.

2.4 PUMP–PROBE SETUP

I described the physical principles of a pump–probe experiment in Section 1.2. This section is concerned with the practical details. Two slightly different setups have been used, a two-color setup (Chapters 5, 6, and 8) and a one-color, polarization-resolved setup (Chapters 4 and 7).

[†]No literature data for the birefringency of sapphire are available. This value applies to ruby (which is very similar) at 707 nm.⁵⁸

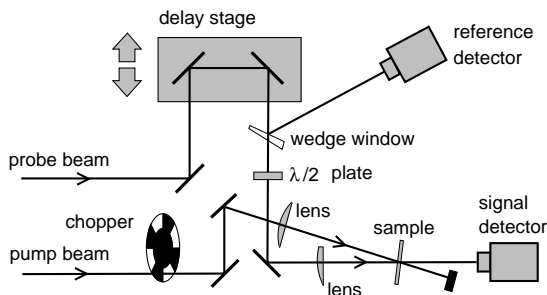
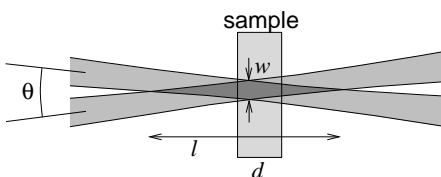


FIGURE 2.3. Pump-probe setup for the experiments in Chapters 5, 6 and 8. The $\lambda/2$ plate rotates the probe pulse polarization to the magic angle (54.7 deg) with respect to the pump pulse polarization.

FIGURE 2.4. Intersection region of the pump and probe beams in the sample. The sample is shown without the sample windows.



2.4.1 TWO-COLOR SETUP

Figure 2.3 shows the two-color pump-probe setup. Calcium fluoride lenses focus the pump and probe pulses into an overlapping region in the sample. A translation stage enables varying the time delay between the pump and probe pulses. A PbSe photoconductive detector measures the energy E_p of the probe pulses after they have passed through the sample; another detector registers, as a reference, the energy of a small fraction of the probe pulse energy E_r that has reflected off a calcium fluoride window. A chopper blocks every other pump pulse, which enables measuring the pulse energies E_p° and E_r° without the effect on the sample of a pump pulse. Thus, the absorbance change

$$\Delta\alpha = -\ln \frac{T}{T^\circ} = -\ln \left(\frac{E_p E_r^\circ}{E_r E_p^\circ} \right) \quad (2.9)$$

is measured as a function of the delay between pump and probe pulses. Around zero delay, we typically achieved $|\Delta\alpha| \approx 0.1$ at 10–20 μJ pump pulse energy.

A zero-order quartz $\lambda/2$ plate rotates the polarization of the probe pulse to the magic angle $\arctan(\sqrt{2}) = 54.7$ deg with respect to the pump pulse polarization. Due to this angle, the reorientational motions of the excited molecules do not affect the absorbance change.

The geometry of the lenses and the sample thickness are a compromise between several considerations. The beam waist diameters w in the pump and probe beam foci and the angle θ between the pump and probe beams lead to an intersection region with a length $l \approx 2w/\theta$ as in Fig. 2.4. Refraction by a sample with index of refraction n will affect both w and θ by a factor $\approx 1/n$, which means that one can substitute the values for w and θ as obtained in air. Since the excitation by the pump pulse temporarily changes the optical

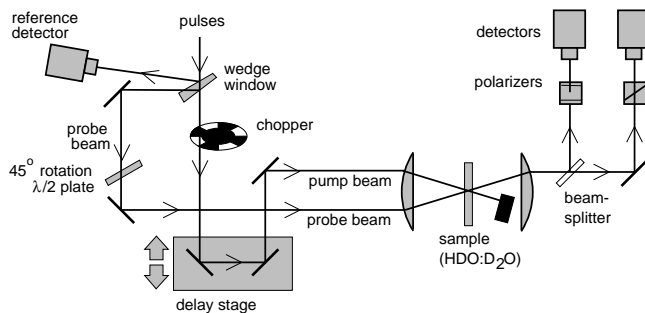


FIGURE 2.5. Pump-probe setup for the experiments in Chapters 4 and 7. In the two-color experiments in Chapter 4, the probe polarization was at the magic angle (54.7 deg), no polarizers were used, and only one detector was placed behind the sample.

properties in the focal region, the probe pulse may not only be partially absorbed, but may also be focused or defocused (due to both diffraction and a change in the index of refraction) compared to the case where no pump pulse was present. This (de)focusing can affect the measured absorbance changes. Therefore, it is important that the probe pulse does not ‘experience’ a strong spatial variation of the optical properties of the sample. From the figure, it is clear that, in order to avoid such edge effects, the length d of the sample should be much shorter than the intersection length l . Also, it is better if the probe beam waist is narrower than the pump beam waist. Further, the necessary angle between the pump and probe beams causes the time resolution to become worse, by roughly $\Delta\tau \approx w\theta/c$. (See Ref. 139 for a detailed calculation.)

In the setup, the lenses have focal lengths of 170 mm (pump) and 100 mm (probe). This results in focal waists of about 100 μm , i.e. typically, 60% of the pump pulse energy and 80% of the probe pulse energy pass through a pinhole with a diameter of 100 μm . With a beam angle $\theta = 0.1$ rad inside the sample, we can estimate that $l \approx 2$ mm and $\Delta\tau \approx 30$ fs. In most experiments, the sample length was $d = 200$ μm . Much shorter lengths would have the disadvantage of a more significant effect of temperature increase as a result of the dissipation of the pump pulse energy (see §2.8). The effect on the time resolution is of minor importance for the pulse durations of typically 200–250 fs in our experiments.

2.4.2 ONE-COLOR POLARIZATION-RESOLVED SETUP

Figure 2.5 shows the pump-probe setup used in the experiments of Chapters 4 and 7. It differs from the setup in §2.4.1 in that the probe pulse is a small fraction of the pump pulse instead of a separately generated pulse, and in that the setup is polarization-resolved. For this purpose, a zero-order quartz $\lambda/2$ plate rotates the probe polarization to 45 deg with respect to the pump pulse polarization. By means of a beamsplitter and two rutile (TiO_2) polarizers, the polarization components parallel and perpendicular to the pump pulse polarization are measured separately. Thus, absorbance changes $\Delta\alpha_{\parallel}$ and $\Delta\alpha_{\perp}$ are measured, from which the isotropic absorbance change and the rotational anisotropy can be calculated. Section 2.7.1 describes how the probe pulse polarization can be extracted

efficiently. In this setup, the focus of the pump and probe pulses is somewhat larger than in the two-color setup of §2.4.1 because a single $f = 100$ mm CaF_2 lens focuses both the pump and probe pulses into the sample. Here, we used $500 \mu\text{m}$ thick samples of an HDO in D_2O solution.

2.5 PULSE CHARACTERISATION

The most important properties of the pulses that were used to carry out the experiments are their duration and their spectrum. Before each pump–probe experiment, we recorded power spectra of both pump and probe pulses using a scanning monochromator (Oriel model MS257) and a PbSe detector. The PbSe detectors and the reflection coefficient of the grating in the monochromator did not have a completely flat frequency response, for which we did not correct. The latter has a minor effect on the measured spectrum, since the frequency response does not vary significantly across an individual power spectrum, which is typically 100 cm^{-1} wide.

In a scan of pump–probe signal versus delay, the instrument function is the correlation function

$$C(t) = \int_{-\infty}^{\infty} I_{\text{pu}}(t')I_{\text{pr}}(t+t')dt' \quad (2.10)$$

of the pump and probe pulses, where $I_{\text{pu}}(t)$ and $I_{\text{pr}}(t)$ are the time-dependent intensities of the pump and probe pulses. We obtained these cross-correlates using the following two methods.

1. Sum-frequency generation (SFG) in a LiIO_4 crystal. The sample was replaced by a LiIO_4 crystal; the overlapping foci of the pump and probe pulses generated sum-frequency light in the case of time-overlap (see §2.1), the intensity of which was detected as a function of delay. This method is accurate, but it has practical disadvantages in the typical situation that pump–probe and cross-correlate measurements are carried out interleaved. The phase-matching for SFG requires polarizations of the pump and probe pulses that are different from in a pump–probe measurement. Due to this phase-matching, the sum-frequency light is emitted in a direction different from the that of the probe pulses, which requires displacing the detectors from their position in a pump–probe experiment. Moreover, the fact that the sum-frequency light has a shorter wavelength than the probe pulses requires replacing spectral filters.
2. Two-photon absorption in germanium. Germanium is transparent for frequencies below 5000 cm^{-1} (Ref. 58) due to its band gap. However, at high intensities, electrons can get excited from the valence band to the conduction band via a two-photon process. If the pump and probe have relatively low intensities, causing only a small amount of two-photon absorption, then it can be shown that the transmittance change $T(t)/T_0 - 1$ of the probe pulses is negative and proportional to $C(t)$. Here, T_0 is the transmittance of the probe pulse in absence of pump pulses. Typically, this technique requires reducing the pulse energies of both pump and probe to ~ 100 nJ. This technique has the advantage of being quick: it requires only replacing the liquid sample by a germanium plate and it does not require adjusting the phase-matching angle. Further, two-photon absorption at high pump intensities creates a population of the

conduction band that causes an increase in absorbance that lasts for many nanoseconds, which enables the experimenter to find the time overlap very rapidly—contrary to sum frequency generation, where both the delay zero point and the phase-matching angle must be adjusted simultaneously in order to obtain any signal. Its disadvantage is a somewhat lower signal-to-noise ratio.

The liquid samples were typically 200 μm thick. Both of the above techniques have the disadvantage that the overlap region (§2.4.1) in the sample is different from that in germanium or LiIO_4 , which are 500 μm and 2 mm thick, respectively. Not only the different lengths of the overlap regions matter, but also the fact that the sample liquid and the cross-correlation material have different dispersive properties. Especially if the pump and probe frequencies are different, dispersion due to different group velocities of the pump and probe introduces an error. Because of this dispersion, we used the cross correlates only to determine the pulse duration and not for the exact delay zero point. In the two-color studies in chapters 5 and 6, the delay zero point was a parameter in the fit procedure. The difference $\Delta t_o = t_{\text{fit}} - t_{\text{cc}}$ between the delay zero points t_{fit} from this fit and t_{cc} from the cross correlate in germanium is roughly proportional to the difference $\Delta\omega = \omega_{\text{pr}} - \omega_{\text{pu}}$ between probe and pump frequencies. The proportionality constant is $\Delta t_o / \Delta\omega \approx 0.78 \text{ fs/cm}^{-1}$ for $\omega_{\text{pr}}, \omega_{\text{pu}}$ in the range 3000–3600 cm^{-1} . We used this relation in Chapter 8.

2.6 REFINEMENTS OF THE PUMP–PROBE SIGNAL DESCRIPTION

The description in §1.2 of vibrational pump–probe signals is a first approximation. An accurate analysis of experimental data requires taking into account a number of additional effects that we have skipped in §1.2. The following list outlines the typical effects that are significant in the studies in this thesis.

1. The pump and pulses are not infinitely short. For realistic pulse durations, we must convolve the signal $\Delta\alpha_\epsilon$ with the instrument response function $C(t)$ described in §2.5.
2. The absorbance change is not measured exactly at frequency ω , but within a frequency distribution defined by the spectrum $f_{\text{pr}}(\omega)$ of the probe pulse. If we assume that $\Delta\alpha \ll 1$ and that the variation of the absorbance $\alpha_o(\omega)$ [Eq. (1.5)] is $\ll 1$ within the probe pulse spectrum, then we can write the experimental pump–probe signal as

$$\Delta\bar{\alpha}_\epsilon(t) = \int d\omega' f_{\text{pr}}(\omega') \int dt' \Delta\alpha_\epsilon(\omega', t - t') C(t'), \quad (2.11)$$

which incorporates point 1 as well.

3. The cross-section spectrum $s(\omega' - \omega)$ of an individual OH group is not an infinitely narrow δ function that peaks at frequency ω , but has a certain width, known as the homogeneous linewidth. For optically thin samples, it can be shown that homogeneous broadening is equivalent to replacing the pump and probe spectra by the convolutions $F_{\text{pr,pu}}(\omega) = f_{\text{pr,pu}}(\omega) * s(\omega)$.

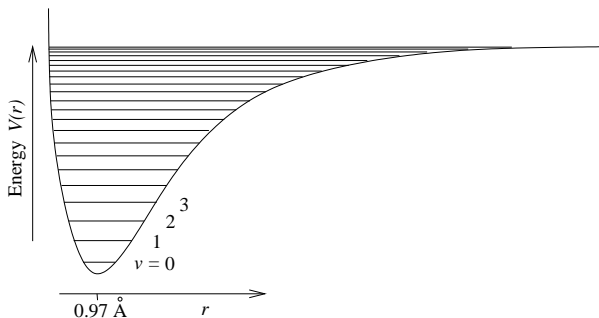


FIGURE 2.6. Schematic potential of the OH stretch vibration, as a function of the O–H distance r . The distance between subsequent energy levels decreases with increasing quantum number ν . This potential applies to gas phase OH groups that have no hydrogen-bonds interactions. The case with hydrogen bonds is discussed in Chapter 8.

4. The excited state and the ground state have different spectra. Typically, subsequent energy levels of a molecular vibration are not spaced uniformly, as is shown in Fig. 2.6, which means that the presence of excited OH groups results in a negative absorbance change (bleaching) at the frequency corresponding to the $\nu = 0 \rightarrow 1$ transition, and in a positive absorbance change (induced absorbance) at the frequency corresponding to the $\nu = 1 \rightarrow 2$ transition. The frequency difference is called the anharmonic redshift $\delta\omega_{\text{anh}}$, which has a value of 270 cm^{-1} (Ref. 45 and Chapter 8). Further, the relation between the hydrogen bond and the OH stretch frequency causes the $\nu = 1$ population to contribute to the bleaching at a slightly different frequency than the depletion of the $\nu = 0$ population. This Stokes shift will be discussed in detail in Chapter 5 and will be used in later chapters. Finally, the value of the anharmonic redshift is in a complicated manner related to the hydrogen-bond interactions, an issue that is treated in Chapter 8.
5. The linear relationship [Eq. (1.6)] between the excited-state population $f_x(\omega, t)$ and the absorbance change $\Delta\alpha_e(\omega, t)$, corrected for the pulse duration and bandwidths (points 1 and 2) only holds if the time evolution of f_x is relatively slow. Slow means that $\tau_c\Delta_m \gg 1$, where Δ_m is the bandwidth over which spectral modulation occurs and τ_c is the correlation time of the spectral modulation. Except for Chapter 7, the studies in this thesis assume the limit $\tau_c\Delta_m \gg 1$.[♯]

The above refinements are in a sense trivial and will be used during the analysis of the experiments when necessary. However, there are two effects that must be described in a different language. Around $t = 0$, the temporal overlap between the pump and probe pulses can cause contributions to the pump–probe signal that are not described by Eq. (1.6). Because these extra signals are only indirectly related to the dynamics of the OH groups, and because they depend in a complicated way on parameters that may or may

[♯]For $\tau_c\Delta_m \lesssim 1$, the spectral width of $\Delta\alpha_e$ would be smaller than the width of f_x . For $\tau_c\Delta_m \ll 1$, the system becomes homogeneously broadened (item 3). We assume here that spectral modulation can be interpreted as an oscillating spring whose force constant is randomly modulated, without jumps in the phase of the oscillation. See for example Buhrstein¹³ for a theoretical treatment on the effects of various types of spectral modulation.

not be known, these extra signal contributions are often referred to as *artifacts*.

6. The *coherent artifact*, that occurs when the pump and probe pulses have overlapping spectra and that appears as a narrow (less than the pulse duration) peak centered at $t = 0$. During time overlap, the simultaneous presence of the pump and probe fields causes an interference pattern in the sample and hence a corresponding spatial pattern of the sample transmittance. The latter acts as a grating that diffracts pump light into the propagation direction of the probe beam, thus causing an additional negative contribution to $\Delta\alpha$. The effect (i.e. the product of amplitude and duration of the artifact) is strongest when strongly coherent (Fourier transform limited) pulses are used. The magnitude of the effect may be calculated, but the calculation is rather involved and requires knowledge about the spectral broadening mechanisms and the degree of coherence of the laser pulses.^{88,131} It appears, however, that the coherent artifact is not very significant in the experiments described in this thesis. For example, the transient spectra of HDO:D₂O in Chapter 8 can be described without incorporating a coherent artifact.
7. The *cross-phase modulation (XPM) artifact*, in which the spectrum of the probe pulses changes slightly due to the simultaneous presence of the electric field of the pump pulse. The index of refraction effectively changes slightly due to the presence of the intense pump field. This coupling is called the optical-field-induced birefringence.¹⁰⁹ Depending on whether this change occurs predominantly in the head (delay $t < 0$) or tail ($t > 0$) of the probe pulses, the result is a small shift $\delta\omega_{\text{pr}}(t)$ of the spectrum that is negative or positive, respectively. Equation (30) in Ref. 60 describes the relative change in spectral intensity for the case of transform-limited pump and probe pulses that applies to the typical pump intensities in the experiments in this thesis, but is limited to cases with negligible differences in group velocity between pump and probe (e.g. $|\omega_{\text{pu}} - \omega_{\text{pr}}| < 100 \text{ cm}^{-1}$). At higher pump intensities, or with significant group-velocity differences between pump and probe (as is the case with two-color experiments), a numerical approach is necessary to calculate the XPM artifact.²⁶ Cross-phase modulation can occur both in the sample and in the sample window before the sample (in the window behind the sample, the pump intensity is too low to be significant). The amplitude of the XPM artifact depends further on the coupling constant (i.e., one of the tensor elements of $\chi^{(3)}$) in the windows and in the sample medium and on the geometry of the spatial overlap region of the pump and probe beams. In the experiments in this thesis, the maximum amplitude of the shift $\delta\omega_{\text{pr}}$ is small ($< 2 \text{ cm}^{-1}$ as measured in CaF₂), but if the transmittance of the sample changes steeply with frequency, the result is that the spectrally shifted pulse undergoes a different attenuation different from what the original pulse would have had. For narrow pulse spectra, we can approximate the XPM contribution to the absorbance change $\Delta\alpha$ as

$$\Delta\alpha_{\text{XPM}}(\omega, t) = \frac{d\alpha_o}{d\omega} \delta\omega_{\text{pr}}(t) \quad (2.12)$$

where ω is the probe frequency and α_o is the linear absorption spectrum [Eq. (1.5)]. Because of the large number of parameters whose values are difficult to obtain, the exact magnitude is difficult to calculate, but if group velocity dispersion can be neglected,

$\delta\omega_{\text{pr}}$ has a behavior similar to

$$\delta\omega(t) \approx kE_{\text{pu}}g'(t), \quad (2.13)$$

where g' is the derivative of a Gaussian with unit amplitude and a width comparable to the width of the instrument function $C(t)$ (§2.5) and k is a proportionality constant. It is clear that the XPM artifact will be reduced if the absorbance of the sample is not chosen too high: the artifact contribution $\Delta\alpha_{\text{XPM}}$ is proportional to the sample absorbance $\Delta\alpha_0$, while the pump–probe signal is proportional to $1 - T_0 = 1 - \exp(-\alpha_0)$. Further, the XPM artifact is especially significant if the desired bleaching signal is very weak.

In principle, pump–probe signals can be described with a much more rigorous mathematical formalism,^{8,88} which incorporates the effects under points 1–3, 5, and 6. Because the coherent artifact is a natural result of this formalism, the term ‘artifact’ is sometimes considered inappropriate. However, that the formalism is more rigorous cannot compensate for the fact that it depends on the same unknown or difficult to obtain parameters under 3, 5, and 6. Even very general expressions for a pump–probe signal, that can only be evaluated after some approximations, depend on some assumptions that tend to be obscured by the mathematical details.

2.7 NOISE SUPPRESSION

The parametric generation and amplification process that we use to obtain infrared pulses, is inherently a source of noise in the signals being measured. Since the conversion process depends highly nonlinearly on the energy of the pump pulses, any fluctuations in the 800-nm pump energy show up as large variations in the energy of the infrared pulses at $3\ \mu\text{m}$. It is not uncommon to observe an individual pulse energy that differs by 30% from the average pulse energy. In addition, the power spectrum and the beam profile can vary slightly from pulse to pulse. Finally, in an experiment where the sample is rotated to reduce the effects of accumulated local heating, a small inhomogeneity, e.g. in the thickness, of the sample may cause the sample transmittance to oscillate with a few Hertz. Hence, it is important to design the experiment such that an optimal signal-to-noise ratio is achieved. I will discuss two limiting cases.

2.7.1 UNCORRELATED NOISE

Uncorrelated noise is noise of a completely random nature that varies randomly from pulse to pulse and possibly from detector to detector. This may originate from fluctuations in the pulse energy or from the detector electronics. In order to correct for energy fluctuations, we use one detector to measure the energies of the pulses in the reference beam. In the case of the laser shots where a pump pulse is present, this yields reference energies r_i , where the subscript $i = 1, \dots, N$ indicates the individual pulses. A detector behind the sample acquires the energies p_i of the probe pulses. For the laser shots without a pump pulse, the energies are r_i° and p_i° . The corresponding transmittances are $T_i = p_i/r_i$ and $T_i^\circ = p_i^\circ/r_i^\circ$. (Formally, this is not correct if the detectors have different efficiencies.

However, this does not affect the ratio T_i/T_i° .) Commonly, the absorbance change is calculated as $\Delta\alpha = -\ln(\langle T_i \rangle / \langle T_i^\circ \rangle)$ or $\Delta\alpha = -\ln(\langle T_i/T_i^\circ \rangle)$. Unfortunately, any noise in the detector signals will affect the ratio p_i/r_i more strongly for pulses with a weaker energy. In these equations, all laser shots are assigned equal weights, which causes excessive noise in $\Delta\alpha$ due to pulses with low energies. Therefore, we calculate $\Delta\alpha = -\ln(T/T^\circ)$, where T and T° result from a linear least-squares fit of $p_i = Tr_i$ and $p_i^\circ = T^\circ r_i^\circ$ to the data, as is shown in Fig. 2.7. If we assume that the error is unknown, but equal for each data point, a linear least squares fit of the parameter T in $p = Tr$ results in

$$T = \frac{\sum_i p_i^2}{\sum_i r_i p_i}, \quad (2.14)$$

$$\sigma_p = \left(\frac{\sum_i p_i^2 + 2T \sum_i r_i p_i + T^2 \sum_i r_i^2}{N - 1} \right)^{\frac{1}{2}}, \quad (2.15)$$

$$\sigma_T = \sigma_p / \sqrt{\sum_i r_i^2}, \quad (2.16)$$

where σ_T and σ_p are the errors in T and in p , respectively. These result from the assumption that a good error estimate should result in

$$\chi^2 \equiv \sum_i \sigma_p^{-2} (p_i - Tr_i)^2 \approx N - 1. \quad (2.17)$$

Using Eq. (2.14) leads to a strong reduction in the noise in $\Delta\alpha$ compared to the more naïve methods mentioned in the beginning of this section.

In polarization-resolved experiments (Chapter 7), separate detectors measure the probe pulse energies for parallel and perpendicular polarizations, which results in $\Delta\alpha_{\parallel}$ and $\Delta\alpha_{\perp}$ from the same procedure as above. In the polarization-resolved experiments, we measured the quantity

$$A = \frac{\Delta\alpha_{\parallel} - \Delta\alpha_{\perp}}{\Delta\alpha_{\parallel} + 2\Delta\alpha_{\perp}}. \quad (2.18)$$

In this case, we can reduce the noise even more by observing that, for a single laser shot, we can write the numerator as

$$\Delta\alpha_{\parallel,i} - \Delta\alpha_{\perp,i} = -\ln \left(\frac{p_{\parallel,i}}{p_{\perp,i}} \cdot \frac{p_{\perp,i}^\circ}{p_{\parallel,i}^\circ} \right). \quad (2.19)$$

which is now not influenced by any noise in the reference signals r_i . Using similar arguments as for T/T° , we calculate the quantities D and D° , that represent the ratios of the signals measured by the parallel and perpendicular detectors, by fitting the functions $p_{\parallel} = Dp_{\perp}$ and $p_{\parallel}^\circ = D^\circ p_{\perp}^\circ$. We can now express the rotational anisotropy [Eq. (2.18)] as

$$A = \frac{-\ln(D/D^\circ)}{\Delta\alpha_{\parallel} + 2\Delta\alpha_{\perp}}. \quad (2.20)$$

We found that the above techniques improved our signal-to-noise ratio by almost an order of magnitude, compared to mere averaging of the detector responses.

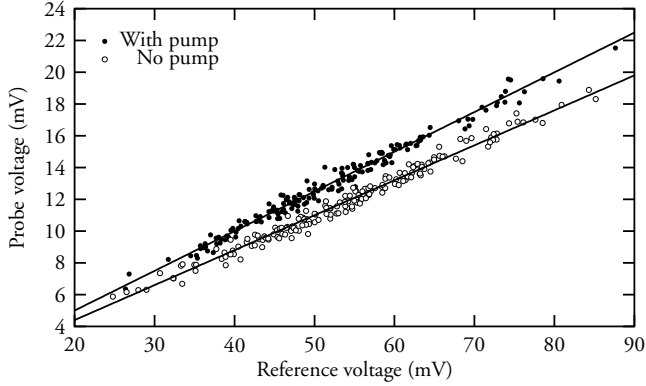


FIGURE 2.7. Typical detector responses for the component of the probe polarization that is parallel to the pump polarization. The lines are linear least-squares fits to the data, with slope $T = \sum_i p_{w,i} r_i / \sum_i r_i^2$ (similar for T_o).

2.7.2 TIME-CORRELATED NOISE

In the case where the laser shows slow fluctuations or the sample transmittance fluctuates due to an inhomogeneous sample that is rotated, the method in §2.7.1 is not optimal. Typically, we handle data sets with size $N \sim 10^3$ points that are acquired during a few consecutive seconds. Equation (2.14) ignores the fact that the sample transmittance is nearly equal for two consecutive laser shots—the sample rotates with a frequency of typically about 2 Hz. On the other hand, we can expect that the quantity of interest, $A \equiv T/T_o$, does not depend significantly on the sample transmittance T_o . In this case, it is better to calculate A and its error σ on a shot-per-shot basis:

$$A_i = \frac{p_i r_i^o}{r_i p_i^o}, \quad (2.21)$$

$$\sigma_i = \frac{\sigma_p r_i^o}{(p_i^o)^2 r_i} \sqrt{(p_i^o)^2 + p_i^2}. \quad (2.22)$$

Here, σ_p is the (yet unknown) error in each individual probe pulse energy p_i or p_i^o ; Eq. (2.22) results from standard error propagation in Eq. (2.21). The best estimate $\langle A \rangle$ is now the weighted average

$$\langle A \rangle = \frac{\sum_i \sigma_i^{-2} A_i}{\sum_i \sigma_i^{-2}}, \quad (2.23)$$

with an error

$$\tilde{\sigma}_{\langle A \rangle} = \frac{1}{\sqrt{\sum_i \sigma_i^{-2}}}. \quad (2.24)$$

The tilde indicates that this error is still dependent on the per-shot error σ_p . We can eliminate this by assuming $\sigma_p = 1$ (or any other value) and then calculating the statistical quantity

$$\chi^2 = \sum_i \sigma_i^{-2} (A_i - \langle A \rangle)^2 \quad (2.25)$$

$$= \langle A \rangle^2 \sum_i \sigma_i^{-2} + \sum_i \sigma_i^{-2} A_i^2 - 2\langle A \rangle \sum_i \sigma_i^{-2} A_i. \quad (2.26)$$

Since, as in the previous section, a good error estimate should result in $\chi^2 \approx N - 1$, the error in $\langle A \rangle$ is

$$\sigma_{\langle A \rangle} = \bar{\sigma}_{\langle A \rangle} \sqrt{\frac{\chi^2}{N - 1}}. \quad (2.27)$$

For ‘outlier’ data points with small values of either r or p , the expression $T/T_0 = \langle A \rangle$ is unstable, because A can essentially take any value between 0 and infinity. The data weighing in Eq. (2.23) does not entirely compensate for this fact. Further, the summation in Eq. (2.26) is written in a way that allows easy implementation in a computer program, because it does not require storage of all A_i values. However, Eq. (2.26) is somewhat sensitive to roundoff errors if the values of A_i that are averaged differ over many orders of magnitude, which can result in $\chi^2 < 0$. Fortunately, we can easily circumvent this problem by assigning thresholds for r and p and only counting laser shots with r , r_0 , p , and p all above these thresholds.

Compared to the method in the previous section, the present method of calculating T/T_0 can reduce the noise significantly if there are slow fluctuations in the pulse properties or in the sample transmittance. Under circumstances with highly fluctuating pulse energies, it may be a disadvantage that one small value for either r_i^0 , r_i , p_i^0 , or p_i can invalidate the whole expression in Eq. (2.21), which ends up as fewer data points contributing to the final value $\langle A \rangle$.

2.8 THERMAL EFFECTS IN THE SAMPLE

The energy of a pump pulse that is absorbed by the sample does not only lead to a transient absorbance change, but also to a temperature increase in the sample. There are two timescales on which this heating occurs. The faster timescale consists of the thermalization of the vibrational energy, that occurs within picoseconds after the pump pulse. Reference 74 discusses the mechanism of this thermalization. For sample thicknesses of $\sim 200 \mu\text{m}$, this thermalization leads to a very small temperature increase of $\sim 0.2 \text{ K}$, if we assume that $20 \mu\text{J}$ of pump pulse energy is homogeneously dissipated in a volume of $200^2 \times 500 \mu\text{m}^3$, or $\sim 2 \text{ K}$ for a volume of $100^2 \times 200 \mu\text{m}^3$. Because the absorption spectrum of the OH stretch vibration is somewhat dependent on the temperature, this temperature increase affects the delay dependence of the absorbance change by typically 10^{-3} , which is negligible with respect to the signals resulting from bleaching of the OH stretch vibration that are typically 10^{-1} .

The slower timescale results from the diffusion of heat out of the focus of the pump pulse. Because this process is slow compared to the repetition frequency of the laser, the net effect is a build-up temperature increase and gradient in the neighborhood of the focus. Of course, this issue is only relevant for a nonmoving sample, such as used for the experiments in Chapters 6 and 8. I will devote the rest of this section to estimate the magnitude of this effect.

The sample consists of two thick calcium fluoride windows with a thin liquid layer in between, where the energy of the pump pulses is dissipated. We will first consider the simple case of a homogeneous medium. If the medium has a heat conductivity λ , a heat

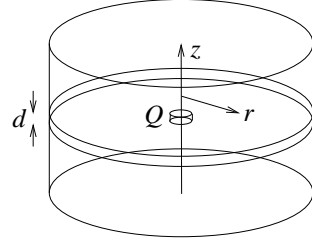


FIGURE 2.8. Geometry of the sample heating. The sample proper has a thickness d ; the heat source Q results from a laser beam that propagates in the z direction.

capacity C per unit volume, and a spherical heat source with power P and radius r_s at the origin, the steady-state temperature $T(r)$ as a function of distance $r > r_s$ from the origin satisfies

$$P = -4\pi\lambda r^2 \frac{dT}{dr}. \quad (2.28)$$

A boundary condition $T(\infty) = T_o$ leads to the solution

$$T(r) = \frac{P}{4\pi\lambda r} + T_o, \quad (2.29)$$

for $r > r_s$. The temperature at the center of the heat source can be obtained by substituting $r = r_s/2$ in Eq. (2.29), as can be shown by refining Eq. (2.28) for $r < r_s$. In water ($\lambda = 0.60 \text{ Wm}^{-1}\text{K}^{-1}$, Ref. 72), a heat source $P = 10 \text{ mW}$ with a radius $r_s = 100 \mu\text{m}$ will therefore lead to a steady-state temperature increase of 27 K. If the medium consists solely of window material (CaF_2 ; $\lambda = 10 \text{ Wm}^{-1}\text{K}^{-1}$, Ref. 58), the same heat source will cause a 1.6 K increase of the steady-state temperature.

The temperature increase in a realistic sample must lie somewhere between these two limiting values. For a quantitative calculation, we choose a cylindrical coordinate system as depicted in Fig. 2.8. The heat diffusion equation for the temperature $T(r, z, t)$ in this geometry is

$$\frac{\partial(CT)}{\partial t} = D \left(\frac{1}{r} \frac{\partial(CT)}{\partial r} + \frac{\partial^2(CT)}{\partial r^2} + \frac{\partial^2(CT)}{\partial z^2} \right) + \frac{\partial D}{\partial z} \frac{\partial(CT)}{\partial z} + Q, \quad (2.30)$$

where $D(z) \equiv \lambda(z)/C(z)$ is the position-dependent diffusion constant and $Q(r, z)$ is the heat source. We assume that

$$Q(r, z) = Q_o \exp\left(-\frac{r^2}{2r_o^2} - \alpha z\right) \quad (0 < z < d), \quad (2.31)$$

where r_o corresponds to an FWHM of $100 \mu\text{m}$ and $\alpha = -\ln(T_o)/d$ is the extinction coefficient that corresponds to a transmittance $T_o = 0.05$ with a sample thickness $d = 200 \mu\text{m}$. We choose Q_o such that the total dissipated power is 10 mW , which corresponds to $20 \mu\text{J}$ pump pulses at a repetition rate of 500 Hz (due to chopping). For a water sample, $C = 4.18 \times 10^6 \text{ Jm}^{-3}\text{K}^{-1}$ (Ref. 72); for the calcium fluoride windows, $C = 2.70 \times 10^6 \text{ Jm}^{-3}\text{K}^{-1}$ (Ref. 58). A simple forward time centered space (FTCS) algorithm¹⁰⁰ was used to integrate Eq. (2.30), with step sizes $\delta r = \delta z = 0.01 \text{ mm}$, $\delta t = 6.25 \mu\text{s}$. The boundary conditions were

$$T(r_{\max}, z, t) = T(r, -z_{\max}, t) = T(r, d + z_{\max}, t) = 0, \quad (2.32)$$

$$T(r, z, 0) = 0, \quad (2.33)$$

FIGURE 2.9. Calculated equilibrium temperature distribution (relative to the temperature at $r, z \rightarrow \infty$) in a CaF_2 sample cell for a 10-mW heat source. The shaded area indicates the sample (200 μm water). Subsequent contour lines correspond to temperatures that differ by a factor $10^{1/12}$. Temperatures are in K. The highest relative temperature is 11.0 K.

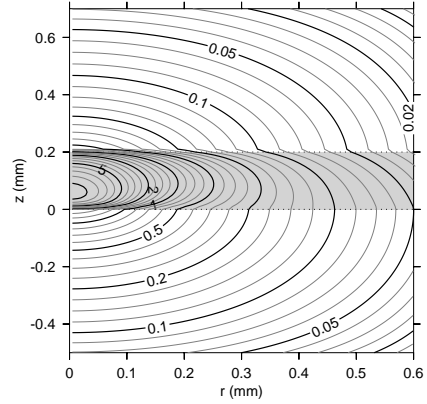


TABLE 2.1. Maximum temperature increases in the focus for a water sample with CaF_2 or sapphire windows at a dissipated power $Q = 10 \text{ mW}$, for various sample thicknesses d and focus radii r_o . In sapphire, $C = 3.0 \times 10^6 \text{ Jm}^{-3}$ and $\lambda = 34 \text{ Wm}^{-1}\text{K}^{-1}$.⁵⁸

r_o (mm)	d (mm)	$T_{\text{max, CaF}_2}$ (K)	$T_{\text{max, sapphire}}$ (K)
0.03	0.03	12.8	10.5
0.03	0.05	15.9	14.0
0.03	0.10	17.9	16.5
0.03	0.20	17.5	16.6
0.03	0.50	13.4	13.1
0.05	0.03	6.2	4.7
0.05	0.05	8.0	6.7
0.05	0.10	10.1	9.1
0.05	0.20	11.1	10.5
0.05	0.50	9.5	9.3
0.10	0.03	2.2	1.5
0.10	0.05	2.8	2.1
0.10	0.10	3.9	3.4
0.10	0.20	5.1	4.7
0.10	0.50	5.3	5.1

with $r_{\text{max}} = z_{\text{max}} = 0.8 \text{ mm}$.⁵⁹ There exist algorithms to calculate the steady-state solution more efficiently¹⁰⁰ than by the FTCS algorithm, but the latter requires relatively limited programming effort. Figure 2.9 shows the temperature distribution at $t = 1 \text{ s}$, which is very close to equilibrium, given that the equilibration time is 45 ms for this set of parameters. Table 2.1 shows the maximum temperature increases for some other parameter combinations.

⁵⁹The first term inside the brackets of Eq. (2.30) needs special attention, because it is undefined at $r \leq 0$. If $r_j = (j + 1/2)\delta r$, then for $j = 0$, the sum of the first two terms can be written as $2C(\delta t/\delta r^2)(T_i - T_o)$, which is well-defined.